

Current-induced spin-orbit torque on the surface of a transition metal dichalcogenide connected to a two-dimensional ferromagnet CrI₃: Effects of twisting and gating

Leyla Majidi,^{1,2,*} Azadeh Faridi,² and Reza Asgari²

¹Department of Physics, Faculty of Science, Shahid Chamran University of Ahvaz, Ahvaz, Iran

²School of Quantum Physics and Matter, Institute for Research in Fundamental Sciences (IPM), P.O. 19395-5531, Tehran, Iran

(Dated: August 1, 2025)

Motivated by recent progress in employing two key classes of two-dimensional materials-topological insulators and transition-metal dichalcogenides (TMDCs)-as spin sources for generating spin-orbit torque (SOT), we investigate current-induced spin polarization and the resulting SOT in bilayers composed of a TMDC (WSe₂ or MoSe₂) and ferromagnetic chromium iodide (CrI₃), beyond the linear response regime. Using the steady-state Boltzmann equation, we find that intra-band transitions yield a strong field-like torque on the CrI₃ layer, while inter-band transitions give rise to a comparatively weaker damping-like torque in the WSe₂/CrI₃ system. Remarkably, the damping-like component is enhanced by up to three orders of magnitude in n-doped MoSe₂, reaching a strength comparable to the field-like torque, which itself is an order of magnitude larger than that in the WSe₂-based bilayer. Both torque components exhibit strong asymmetry between n-type and p-type doping in WSe₂ and MoSe₂ systems. Furthermore, we demonstrate that the twist angle plays a crucial role: depending on the TMDC and chemical potential, twisting can reverse the sign of the SOT and significantly modulate its magnitude. Finally, we show that a transverse gate electric field enables substantial tunability of the SOT, by nearly one order of magnitude, and induces a sign reversal at a twist angle of 10.16°.

I. INTRODUCTION

Magnetization manipulation and switching mediated by spin torques is the central goal in memory and logic spintronic devices. This has been conventionally achieved by transferring spin angular momentum from a ferromagnetic fixed layer to a ferromagnetic free layer separated by a non-magnetic spacer applying a perpendicular electric field (spin transfer torque)^{1–6}. In recent years, an alternative mechanism for generating spin torques has been predicted in non-magnetic/ferromagnetic bilayers which is based on producing a transverse spin current in the nonmagnetic layer with a strong spin-orbit coupling applying an in-plane electric field. The interface-generated spin current arises from spin-orbit filtering and spin-orbit precession mechanisms⁷, and leads to an accumulation of spins at the interface producing a spin torque, the so-called spin-orbit torque (SOT), which can in turn manipulate the magnetic moments in the ferromagnetic layer^{8,9}. The spin-orbit filtering current exhibits a fixed spin-polarization direction \mathbf{S} and generates a torque given by $\mathbf{m} \times (\mathbf{m} \times \mathbf{S})$ on the local magnetization vector \mathbf{m} . In contrast, the spin-orbit precession current possesses a magnetization-dependent spin polarization, expressed as $\mathbf{m} \times \mathbf{S}$, and produces a torque of the form $\mathbf{m} \times (\mathbf{m} \times [\mathbf{m} \times \mathbf{S}]) = \mathbf{m} \times (-\mathbf{S})$. Generally, these spin torques are classified as damping-like [$\tau_{DL} \propto \mathbf{m} \times (\mathbf{m} \times \mathbf{S})$] and field-like ($\tau_{FL} \propto \mathbf{m} \times \mathbf{S}$), respectively⁹.

Search for source materials with a strong spin-orbit coupling for generating spin-orbit torques have been the subject of an intense study for almost two decades. Large spin-orbit torques have been predicted and observed in a variety of bilayer systems with heavy metal/ferromagnet (HM/FM) and topological insulator/ferromagnet (TI/FM) as the most conventional heterostructures. Considerable spin-orbit torques resulting from strong spin-orbit interaction at both bulk and the interface of HM/FMs with W, Pt and Ta as the most

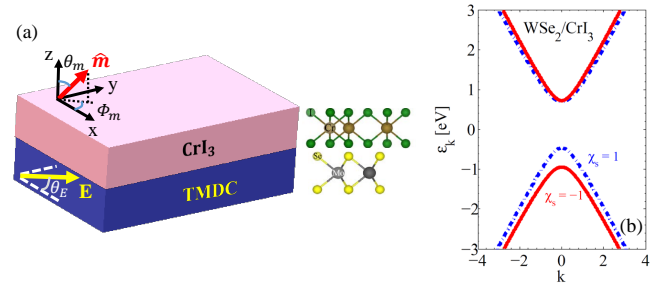


FIG. 1. (Color online)(a) Schematic of a TMDC/CrI₃ bilayer with a magnetization direction $\mathbf{m} = (\sin \theta_m \cos \phi_m, \sin \theta_m \sin \phi_m, \cos \theta_m)$. There is an applied electric field, $\mathbf{E} = |E|(\cos \theta_E, \sin \theta_E, 0)$, at the interface of TMDC/CrI₃ along $x - y$ plane. (b) The dispersion relation in momentum space of the proposed WSe₂/CrI₃ bilayer at the K valley ($\chi_\tau = 1$).

common metals have been reported^{10–13}. On the other hand, TI/FM bilayers mostly based on Sb and Bi chalcogenides have also shown much larger SOT efficiencies with respect to HM/FM bilayers due to the spin-momentum locking of the surface states of topological insulators^{14–17}.

Transition metal dichalcogenides (TMDCs) are considered as another promising candidate materials for producing sizable SOT in TMDC/FM bilayers due to their strong intrinsic spin-orbit coupling and diverse symmetry features^{18–21}. The distinct properties of these materials can lead to large charge-to-spin conservation efficiencies and out-of-plane SOTs which are desirable for switching the magnets in bilayers with perpendicular magnetic anisotropy. The large diversity of TMDC materials with different crystalline symmetries and subsequent diverse band structures can lead to diverse spin-orbit torques with conventional and unconventional orientations. In recent years, an increasing number of experimental observations of SOT in several TMDC-based heterostructures have

been reported: such as WTe_2 ^{22–24} and TaTe_2 ^{25,26}, MoS_2 ^{27,28} and WSe_2 ^{28–30}, NbSe_2 ³¹ and TaS_2 ³² with respectively semi-metallic, semiconducting and metallic features of TMDCs in combination with a variety of ferromagnetic layers. The different and even discrepant results of these experiments show that not only the TMDC materials with different crystalline symmetries and number of layers can lead to diverse spin-orbit torques with conventional and unconventional orientations, but the ferromagnetic layer can also play an active role in this case³³.

Besides, spin torque is strongly influenced by the symmetry characteristics of the spin-orbit interaction³⁴. In cases where inversion symmetry is preserved- such as impurity-induced spin-orbit interaction or the Luttinger spin-orbit band- the resulting spin torque is a higher-order effect and typically too weak to lead to a reasonable critical switching current density. In contrast, when inversion symmetry is broken, as seen in Rashba and Dresselhaus spin-orbit interactions, the torque emerges as a first-order effect with respect to the SOC parameter and can be effectively utilized to manipulate magnetization direction using relatively low critical switching current densities, on the order of 10^4 to 10^6 A/cm².

An important issue in applying the SOTs realized in heterostructures for practical purposes is the controllability of the size and the orientation of the spin torques. Although there have been observations of the electric field tunable SOTs in HM/FM³⁵, TI/FM¹⁷ and TMDC/FM^{36,37} bilayers and also strain-induced unconventional SOTs³¹, the quest for external modulation of SOT is still underway. In this regard, a recent study shows that in a TMDC/FM bilayer, the proximity exchange in the TMDC monolayer (MoSe_2 or WSe_2) induced by the FM monolayer (CrI_3) is widely tunable via gating and twisting³⁸. This can be a great opportunity to tune the relevant features in this system^{39,40}. As CrI_3 is one of the most interesting two-dimensional (2D) magnets in which the magnetic moment orientation is ferromagnetic in monolayer and antiferromagnetic in bilayer, a large number of studies have been devoted to its special functionalities^{41–44} as well as its intriguing properties when incorporated into TMDCs^{45–51} which stem from the strong proximity effect in these van der Waals (vdW) heterostructures. Several experimental and theoretical studies suggest a strong valley and spin manipulation in TMDC/ CrI_3 bilayer (mostly WSe_2 as TMDC)^{39,40,45–48}. All-optical switching of the magnetization in CrI_3 thin films⁴⁴ and also all-optical control of spin in TMDC/ CrI_3 heterostructures⁵¹ are also reported. On the other hand, a recent study shows that a current-driven proximity-induced SOT emerges in a TaSe_2 /bilayer CrI_3 heterostructure which can switch the direction of the magnetization on the bottom monolayer of CrI_3 to become parallel to that of the top monolayer, thereby converting bilayer CrI_3 from antiferromagnet to ferromagnet⁴⁹.

Motivated by these findings, here we develop a microscopic theory for the current-induced SOT in TMDC/ CrI_3 bilayer (with MoSe_2 or WSe_2 as TMDCs) beyond linear response theory. Of particular interest in this paper is to comment on the tunability of the size and the orientation of the SOT by changing the gate voltage and the twist angle to open a new path

for externally controllable spintronic devices. Employing the single-band steady state Boltzmann equation, we find that the main contribution of the intra-band transitions to the spin polarization is in linear response regime. The spin polarization originating from the electron occupation changes within intra-band transitions generates a strong field-like SOT and the associated intrinsic inter-band transitions contribute to a weak damping-like SOT on the magnetization of the ferromagnetic CrI_3 layer in WSe_2 -based bilayer, exhibiting asymmetric behavior with respect to the chemical potential and sign changing in the case of n-doped MoSe_2 with smaller chemical potentials. Importantly, replacing WSe_2 with MoSe_2 leads to a significant amplification of the strength of the damping-like term (three orders of magnitude) such that it can be approximately at the same order of the field-like term. The strength of the field-like term is also enhanced by an order of magnitude in MoSe_2 in comparison with that of the WSe_2 -based bilayer.

Remarkably, we demonstrate that twisting will result in a significant amplification of the SOT as well as a sign change in MoSe_2 - and p-doped WSe_2 -based bilayers. Moreover, tuning the gate electric field leads to significant enhancement of the strength of the field-like and damping-like SOTs and their sign changes in presence of twisting. Besides, increasing the Rashba spin-orbit coupling enhances the field-like and damping-like SOTs in WSe_2 - and p-doped MoSe_2 -based bilayers, reduces their strengths in n-doped MoSe_2 and eliminate the sign change of the field-like torque.

The rest of the paper is organized as follows. Section II is devoted to the theoretical model and fundamental formalisms which will be implemented to investigate the current-induced spin-orbit torque in a twisted TMDC/ CrI_3 bilayer. We present our numerical results for the non-equilibrium spin polarization and the exerted spin-orbit torque on the magnetization of the ferromagnetic layer in Sec. III. Finally, a brief summary of results is given in Sec. IV.

II. MODEL AND THEORY

The device we consider is a TMDC/ CrI_3 bilayer with monolayer CrI_3 as 2D FM and monolayer WSe_2 or MoSe_2 as TMDC [see Fig. 1]. The magnetic insulator CrI_3 is weakly coupled to the TMDC by vdW forces, preserving the characteristic electronic band structure of the TMDC. The proximity exchange coupling will split the TMDC conduction-band edge by $2B_c$ and the valence-band edge by $2B_v$, and combined with the intrinsic (valley Zeeman) SOC of the TMDC lifts the valley degeneracy. The effective low-energy Hamiltonian which describes the surface of a TMDC in the presence of proximity exchange³⁸, has the form

$$\mathcal{H} = \mathcal{H}_0 + \mathcal{H}_\Delta + \mathcal{H}_{\text{soc}} + \mathcal{H}_{\text{ex}} + \mathcal{H}_R, \quad (1)$$

with

$$\mathcal{H}_0 = \hbar v_F \hat{s}_0 \otimes (\chi_\tau \hat{\sigma}_x k_x + \hat{\sigma}_y k_y), \quad (2)$$

$$\mathcal{H}_\Delta = \frac{\Delta}{2} \hat{s}_0 \otimes \hat{\sigma}_z, \quad (3)$$

$$\mathcal{H}_{soc} = \chi_\tau \hat{s}_z \otimes (\lambda_c \hat{\sigma}_+ + \lambda_v \hat{\sigma}_-), \quad (4)$$

$$\mathcal{H}_{ex} = (\hat{s} \cdot \mathbf{m}) \otimes (B_c \hat{\sigma}_+ + B_v \hat{\sigma}_-), \quad (5)$$

$$\mathcal{H}_R = \lambda_R (\chi_\tau \hat{s}_y \otimes \hat{\sigma}_x - \hat{s}_x \otimes \hat{\sigma}_y). \quad (6)$$

The valley index for the K (K') point is $\chi_\tau = \pm 1$ and v_F represents the Fermi velocity. The pseudospin Pauli matrices $\hat{\sigma}_i$ ($i = 0, x, y, z$) act on the conduction- and valence-band subspaces and \hat{s}_i ($i = 0, x, y, z$) refers to real spin. The parameter Δ denotes the orbital gap of the spectrum. The spin-splittings of the conduction (valence) band due to the intrinsic SOC and the proximity exchange are respectively determined by the parameters $\lambda_{c(v)}$ and $B_{c(v)}$. The local magnetization of the ferromagnetic (F) layer is determined by \mathbf{m} . The Rashba SOC parameter λ_R is due to the presence of inversion asymmetry in the heterostructure. For short notation, we introduce $\hat{\sigma}_\pm = (\hat{\sigma}_0 \pm \hat{\sigma}_z)/2$.

Recently, wide tunability of the proximity exchange in monolayer MoSe₂ or WSe₂ owing to a ferromagnetic monolayer CrI₃ has been explored with respect to twisting and gating^{38,40}. In particular, proximity exchange splitting depends on the twist angle between the TMDC and the CrI₃. Not only do the magnitudes of the exchange differ, but also the direction of the exchange field for the valence band alters sign. When twisting from 0° to 30°, the TMDC conduction band edge splitting remains nearly unchanged at around -3 meV. In contrast, there is a smooth transition of the TMDC valence band edge spin splitting from about -2 to 2 meV (the spin ordering changes). The origin of this reversal is traced back to the twist-angle dependent backfolding of the TMDC K/K' valleys into the CrI₃ Brillouin zone and sensitively depends on the atomic stacking configurations of the strained supercells. Moreover, the proximity exchange parameters increase when the applied transverse electric field is turned from negative to positive values, which enables the gate control of the proximity exchange. We should emphasize that the introduced low-energy model Hamiltonian [Eq. (1)], together with the fitted parameters obtained in Ref. 40, nicely provide an effective description for the TMDC band edges in twisted TMDC/CrI₃ bilayer in the presence of an external electric field. It is worth noting that the gap parameter as well as the Fermi velocity are not affected by external electric fields.

Importantly, large spin-orbit coupling in TMDCs can produce strong enough spin-orbit torque to switch the magnetization of the ferromagnetic layer in TMDC/FM bilayers. The SOT exerting on the ferromagnetic layer, characterized by a local magnetization $\mathbf{m} = (m_x, m_y, m_z) = (\sin \theta_m \cos \phi_m, \sin \theta_m \sin \phi_m, \cos \theta_m)$, has the form

$$\boldsymbol{\tau} = \frac{2J}{\hbar} \mathbf{m} \times \mathbf{S}, \quad (7)$$

with J the exchange energy, $\mathbf{S} = \sum_{\chi} \int \frac{d^2 \mathbf{k}}{(2\pi)^2} \mathbf{s}^\chi(\mathbf{k}) f(\varepsilon_k^\chi)$ the spin polarization with $\mathbf{s}^\chi(\mathbf{k}) = (\hbar/2) \langle \Psi_k^\chi | \hat{\mathbf{s}} | \Psi_k^\chi \rangle$ the spin expectation in the χ -th band with eigenvector Ψ_k^χ and eigenvalue ε_k^χ ,

and $f(\varepsilon_k^\chi)$ the Fermi-Dirac distribution function. The χ -energy band is defined by $\chi = (\chi_\sigma, \chi_s, \chi_\tau)$ in which $\chi_\sigma = \pm 1$ refers to the conduction and valence band subspaces, and $\chi_s = \pm 1$ denotes the two spin-subbands.

Applying an in-plane electric field, parallel to the TMDC/FM interface, leads to the spin polarization $\mathbf{S} = \mathbf{S}^{oc} + \mathbf{S}^{in}$ with \mathbf{S}^{oc} originating from the change of the electron occupation $\delta f(\varepsilon_k^\chi) = f(\varepsilon_k^\chi) - f^{(0)}(\varepsilon_k^\chi)$ within intra-band due to an acceleration by the electric field,

$$\mathbf{S}^{oc} = \sum_{\chi} \int \frac{d^2 \mathbf{k}}{(2\pi)^2} \mathbf{s}^\chi(\mathbf{k}) \delta f(\varepsilon_k^\chi), \quad (8)$$

and

$$\mathbf{S}^{in} = \sum_{\chi} \int \frac{d^2 \mathbf{k}}{(2\pi)^2} \delta \mathbf{s}^\chi(\mathbf{k}) f(\varepsilon_k^\chi), \quad (9)$$

stemming from the modification of the quasiparticle wave functions⁵²⁻⁵⁴, where $\delta \mathbf{s}^\chi(\mathbf{k}) = (\hbar/2) \text{Re} \langle \Psi_k^\chi | \hat{\mathbf{s}} | \delta \Psi_k^\chi \rangle$ can be traced to the inter-band contributions in analogy to the intrinsic contribution to the anomalous Hall effect.

Employing the single-band steady state Boltzmann equation

$$-\frac{e}{\hbar} \mathbf{E} \cdot \nabla_{\mathbf{k}} f(\varepsilon_k^\chi) = -\frac{f(\varepsilon_k^\chi) - f^{(0)}(\varepsilon_k^\chi)}{\gamma(\mathbf{k})}, \quad (10)$$

the n -th order non-equilibrium distribution function in the relaxation time approximation $\gamma(\mathbf{k}) = \gamma$, can be obtained from the recursive relations

$$f^{(n)}(\varepsilon_k^\chi) = \frac{e\gamma}{\hbar} \mathbf{E} \cdot \frac{\partial f^{(n-1)}(\varepsilon_k^\chi)}{\partial \mathbf{k}}. \quad (11)$$

Using this formula, the non-equilibrium distribution function up to the second order can be rewritten as

$$\begin{aligned} f(\varepsilon_k^\chi) &= f^{(0)}(\varepsilon_k^\chi) + f^{(1)}(\varepsilon_k^\chi) + f^{(2)}(\varepsilon_k^\chi), \\ f^{(0)}(\varepsilon_k^\chi) &= [e^{\beta(\varepsilon_k^\chi - \mu)} + 1]^{-1}, \\ f^{(1)}(\varepsilon_k^\chi) &= e\gamma \mathbf{E} \cdot \mathbf{v}^\chi \frac{\partial f^{(0)}(\varepsilon_k^\chi)}{\partial \varepsilon_k^\chi}, \\ f^{(2)}(\varepsilon_k^\chi) &= \frac{e^2 \gamma^2}{\hbar} \left[\mathbf{E} \cdot \frac{\partial (\mathbf{E} \cdot \mathbf{v}^\chi)}{\partial \mathbf{k}} \frac{\partial f^{(0)}(\varepsilon_k^\chi)}{\partial \varepsilon_k^\chi} + \hbar (\mathbf{E} \cdot \mathbf{v}^\chi)^2 \frac{\partial^2 f^{(0)}(\varepsilon_k^\chi)}{\partial (\varepsilon_k^\chi)^2} \right], \end{aligned} \quad (12)$$

with $\mathbf{v}^\chi = \hbar^{-1} \partial_{\mathbf{k}} \varepsilon_k^\chi$ the group velocity of charge carriers, $\mathbf{E} = (E_x, E_y, 0)$ the applied in-plane electric field, $\beta = (k_B T)^{-1}$, k_B the Boltzmann constant, T the temperature and μ the Chemical potential.

First, we calculate the spin polarization stemming from intra-band transitions, using Eq. (8). Diagonalizing the effective Hamiltonian [Eq. (1)], the eigenstates at a given energy ε_k^χ can be obtained as

$$\Psi_k^\chi = A_\chi^{\chi_\tau} e^{i\chi_\tau \chi_\sigma k_x x} e^{i\chi_\sigma k_y y} \begin{pmatrix} \chi_\tau \chi_\sigma N_\chi^{\chi_\tau} e^{-i\chi_\tau \theta} \\ 1 \\ iP_\chi^{\chi_\tau} \\ i\chi_\tau \chi_\sigma M_\chi^{\chi_\tau} e^{i\chi_\tau \theta} \end{pmatrix} \quad (13)$$

Structure	$\Delta[\text{eV}]$	$v_F[10^5 \text{ m/s}]$	$\lambda_c[\text{meV}]$	$\lambda_v[\text{meV}]$	$B_c[\text{meV}]$	$B_v[\text{meV}]$
WSe ₂ /CrI ₃ (no twist)	1.403	5.873	13.81	240.99	-1.460	-0.918
WSe ₂ /CrI ₃ (with twist 30°)	1.477	5.940	13.81	240.99	-1.226	1.525
MoSe ₂ /CrI ₃ (no twist)	1.343	4.358	-9.678	94.43	-1.343	-0.901
MoSe ₂ /CrI ₃ (with twist 30°)	1.401	4.622	-9.678	94.43	-1.176	0.484

TABLE I. The orbital gap Δ , Fermi velocity v_F , spin-orbit coupling $\lambda_{c(v)}$ and the proximity exchange $B_{c(v)}$ of the conduction (valence) band for TMDC/CrI₃ bilayer (with WSe₂ and MoSe₂ as TMDC) in the absence or presence of the twist angle 30° [see Ref. 40]. Notice that B_v changes sign in twisted cases.

for the χ -band with momentum-energy relation

$$|\mathbf{k}_\chi^{\chi_\tau}| = \frac{1}{\sqrt{2}\hbar v_F} [a_1 a_2 + a_3 a_4 - (a_1 + a_2 + a_3 + a_4) \varepsilon_k^\chi + 2 \varepsilon_k^{\chi^2} + \chi_s [(a_1 a_2 - a_3 a_4 + (-a_1 - a_2 + a_3 + a_4) \varepsilon_k^\chi)^2 + 16 (a_{1(2)} - \varepsilon_k^\chi)(a_{4(3)} - \varepsilon_k^\chi) \lambda_R^2]^{1/2}]^{1/2}. \quad (14)$$

Here,

$$N_\chi^+ = \frac{\hbar v_F |\mathbf{k}_\chi^+|}{\varepsilon_k^\chi - a_1},$$

$$P_\chi^+ = \frac{\varepsilon_k^\chi - a_2 - \hbar v_F |\mathbf{k}_\chi^+| N_\chi^+}{2\lambda_R},$$

$$M_\chi^+ = \frac{\hbar v_F |\mathbf{k}_\chi^+| P_\chi^+}{\varepsilon_k^\chi - a_4},$$

and

$$N_\chi^- = \frac{\varepsilon_k^\chi - a_2}{\hbar v_F |\mathbf{k}_\chi^-|},$$

$$M_\chi^- = \frac{N_\chi^- (a_1 - \varepsilon_k^\chi) + \hbar v_F |\mathbf{k}_\chi^-|}{2\lambda_R} e^{-2i\chi_\tau \theta},$$

$$P_\chi^- = \frac{\hbar v_F |\mathbf{k}_\chi^-| M_\chi^-}{\varepsilon_k^\chi - a_3},$$

with superscript \pm denoting the K (K') valley with $\chi_\tau = \pm 1$, $a_{1(3)} = \pm \chi_\tau \lambda_c \pm B_c \cos \theta_m + \Delta/2$, $a_{2(4)} = \pm \chi_\tau \lambda_v \pm B_v \cos \theta_m - \Delta/2$,

$\theta = \arctan(k_y/k_x)$, and $A_\chi^{\chi_\tau} = (|N_\chi^{\chi_\tau}|^2 + |P_\chi^{\chi_\tau}|^2 + |M_\chi^{\chi_\tau}|^2 + 1)^{-1/2}$. Note that the azimuthal angle ϕ_m is set to zero.

Using Eqs. (13) and (14), the spin expectation components are obtained as follows,

$$s_x^\chi = -\hbar \chi_\tau \chi_\sigma |A_\chi^{\chi_\tau}|^2 [\text{Im}(N_\chi^{\chi_\tau*} P_\chi^{\chi_\tau} e^{i\chi_\tau \theta}) + \text{Im}(M_\chi^{\chi_\tau} e^{i\chi_\tau \theta})] \quad (15)$$

$$s_y^\chi = \hbar \chi_\tau \chi_\sigma |A_\chi^{\chi_\tau}|^2 [\text{Re}(N_\chi^{\chi_\tau*} P_\chi^{\chi_\tau} e^{i\chi_\tau \theta}) + \text{Re}(M_\chi^{\chi_\tau} e^{i\chi_\tau \theta})] \quad (16)$$

$$s_z^\chi = \hbar |A_\chi^{\chi_\tau}|^2 (|N_\chi^{\chi_\tau}|^2 - |P_\chi^{\chi_\tau}|^2 - |M_\chi^{\chi_\tau}|^2 + 1)/2. \quad (17)$$

Also, the non-equilibrium distribution functions can be written in terms of the excitation energy, $\varepsilon = \varepsilon_k^\chi - \mu$, as follows

$$f^{(0)}(\varepsilon) = [e^{\beta\varepsilon} + 1]^{-1}, \quad (18)$$

$$f^{(1)}(\theta, \varepsilon) = -\beta\gamma e|\mathbf{E}|(v_x^\chi \cos \theta_E + v_y^\chi \sin \theta_E) e^{\beta\varepsilon} [f^{(0)}(\varepsilon)]^2, \quad (19)$$

$$f^{(2)}(\theta, \varepsilon) = (\beta\gamma e|\mathbf{E}|)^2 [(\partial v_x^\chi / \partial k_x) \cos^2 \theta_E + (\partial v_y^\chi / \partial k_y) \sin^2 \theta_E + (\partial v_x^\chi / \partial k_y + \partial v_y^\chi / \partial k_x) \cos \theta_E \sin \theta_E] (\partial f^{(0)}(\varepsilon) / \partial \varepsilon) + [v_x^\chi \cos \theta_E + v_y^\chi \sin \theta_E]^2 (\partial^2 f^{(0)}(\varepsilon) / \partial \varepsilon^2), \quad (20)$$

with $\mathbf{v}^\chi = \chi_\sigma [\hbar |\mathbf{k}_\chi(\varepsilon)| \partial |\mathbf{k}_\chi(\varepsilon)| / \partial \varepsilon]^{-1} (k_x, k_y) = \chi_\sigma [\hbar \partial |\mathbf{k}_\chi(\varepsilon)| / \partial \varepsilon]^{-1} (\cos \theta, \sin \theta)$, $\chi_\sigma = \text{sgn}(\mu + \varepsilon)$, $\theta_E = \arctan(E_y/E_x)$, and $|\mathbf{E}| = \sqrt{E_x^2 + E_y^2}$.

Finally, the intra-band spin polarization \mathbf{S}^{oc} in response to an in-plane applied electric field, and the resulting spin-orbit torque $\boldsymbol{\tau}^{oc} = 2J\hbar^{-1} \mathbf{m} \times \mathbf{S}^{oc}$, exerting on the ferromagnetic layer characterized by a local magnetization $\mathbf{m} = (\sin \theta_m, 0, \cos \theta_m)$ and J the exchange energy, can be obtained using

$$\mathbf{S}^{oc} = \left(\frac{1}{2\pi}\right)^2 \sum_\chi \int_0^\infty d\varepsilon |\mathbf{k}_\chi^\tau(\varepsilon)| \frac{\partial |\mathbf{k}_\chi^\tau(\varepsilon)|}{\partial \varepsilon} s^\chi(\varepsilon) \int_0^{2\pi} d\theta [f^{(1)}(\theta, \varepsilon) + f^{(2)}(\theta, \varepsilon)]. \quad (21)$$

The contribution of the linear $S^{oc(1)}$ and non-linear $S^{oc(2)}$ terms to the intra-band spin polarization S^{oc} are presented in Fig. 2(b). We find that the contribution of the non-linear term $S^{oc(2)}$ is 10^{-4} times smaller than that of the linear term. Therefore, the spin polarization S^{oc} and the resulting spin-orbit torque mainly arise from the linear term.

Then, we evaluate the contribution of the intrinsic inter-band transitions on the spin polarization in the linear response regime, by making use of Eq. (9). Following the perturbation method to find the modifications in the wave function, we have^{52–54}

$$S^{in} = \frac{e\hbar^2}{A} \sum_{\chi \neq \chi', \mathbf{k}} [f^{(0)}(\epsilon_{\mathbf{k}}^{\chi}) - f^{(0)}(\epsilon_{\mathbf{k}}^{\chi'})] \frac{\text{Im}[\langle \Psi_{\mathbf{k}}^{\chi} | \hat{s} | \Psi_{\mathbf{k}}^{\chi'} \rangle \langle \Psi_{\mathbf{k}}^{\chi'} | \hat{v} \cdot \mathbf{E} | \Psi_{\mathbf{k}}^{\chi} \rangle]}{(\epsilon_{\mathbf{k}}^{\chi} - \epsilon_{\mathbf{k}}^{\chi'})^2} \quad (22)$$

for each valley with $\hat{v} = \hbar^{-1} \partial_{\mathbf{k}} \mathcal{H}$.

Finding the imaginary part on the right hand side (rhs) of the above equation and performing the integration over θ , we find $S_{z\chi\tau}^{in} = 0$ and the x and y contributions of the intrinsic term of the spin polarization are given by

$$S_{x(y)}^{in} = (2\pi e v_F \hbar^2) \chi_{\tau} \sum_{\chi \neq \chi'} \int dk d\mathbf{k} \frac{[f^{(0)}(\epsilon_{\mathbf{k}}^{\chi}) - f^{(0)}(\epsilon_{\mathbf{k}}^{\chi'})]}{(\epsilon_{\mathbf{k}}^{\chi} - \epsilon_{\mathbf{k}}^{\chi'})^2} (A_{\chi}^{\chi\tau} A_{\chi'}^{\chi\tau})^2 (\alpha^{\chi\tau} \beta'^{\chi\tau} - \beta^{\chi\tau} \alpha'^{\chi\tau}) E_{x(y)}, \quad (23)$$

where $\alpha^{\chi\tau} = (N_{\chi}^{\chi\tau} P_{\chi'}^{\chi\tau} + M_{\chi'}^{\chi\tau})$, $\beta^{\chi\tau} = (P_{\chi}^{\chi\tau} N_{\chi'}^{\chi\tau} + M_{\chi}^{\chi\tau})$, $\alpha'^{\chi\tau} = (M_{\chi}^{\chi\tau} P_{\chi'}^{\chi\tau} + N_{\chi'}^{\chi\tau})$, and $\beta'^{\chi\tau} = (P_{\chi'}^{\chi\tau} M_{\chi}^{\chi\tau} + N_{\chi}^{\chi\tau})$.

III. NUMERICAL RESULTS AND DISCUSSION

In this section, we present our numerical results for the current-induced spin-orbit torque exerted on the magnetization of the ferromagnetic layer. Before presenting our numerical results, it is worth noting that the orbital gap Δ , spin-orbit coupling $\lambda_{c(v)}$, and the exchange interaction $B_{c(v)}$ parameters for different TMDCs (like WSe₂ and MoSe₂), in the absence or presence of twisting are set to the values obtained in Ref. 40 [see Table. I for the twist angles 0° and 30°]. It has been shown that the absence or presence of the SOC term in the bilayer calculations does not lead to significant changes in the magnitude of the exchange parameters. However, twisting the CrI₃ layer relative to the WSe₂ (MoSe₂) changes the sign of the exchange field in the valence band around 16° (8°) and makes the valence-band spin-splitting opposite in sign in the absence of SOC. Therefore, twisting can remain an effective tool to modify the proximity exchange field.

The chemical potential μ is in units of electron volt (eV). For practical applications in electronic devices, the single-layer and multi-layer TMDCs can be n - or p -doped on generating desirable charge carriers^{55–57}. We set the relaxation time $\gamma = 3$ ps, the magnitude of the in-plane electric field

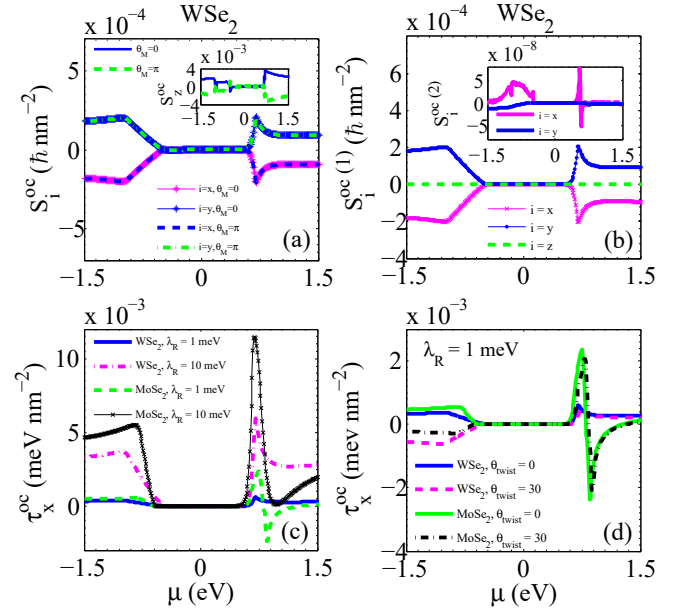


FIG. 2. (Color online) (a) Chemical potential dependence of the non-equilibrium intra-band spin polarization S^{oc} components in WSe₂/CrI₃ bilayer for two magnetization directions $\theta_m = 0$ and π , when $\lambda_R = 1$ meV, $\theta_{twist} = 0^\circ$ and $\theta_E = \pi/4$. (b) The contribution of the linear $S^{oc(1)}$ and non-linear $S^{oc(2)}$ terms of the spin polarization components, when $\theta_m = 0$. (c) The x -component of the spin-orbit torque τ_x^{oc} in terms of the chemical potential μ in the absence and presence of twisting ($\theta_{twist} = 30^\circ$) for WSe₂- or MoSe₂- based bilayer, when $\theta_m = 0$. Note that we have $\tau_y^{oc} = \tau_x^{oc}$ in the case of $\theta_E = \pi/4$. (d) The behavior of the x -component of S^{oc} in terms of μ for two values of Rashba SOC in untwisted WSe₂- or MoSe₂-based bilayer, when $\theta_m = 0$.

$E = 0.2$ mV/nm, $k_B T = 25.7$ meV for room temperature, and replace the exchange parameter J with $B_{c(v)}$ for the conduction (valence) band.

A. Spin-orbit torque from intra-band transitions

Figure 2(a) shows the behavior of the current-induced spin polarization S^{oc} components stemming from the intra-band transitions in terms of the chemical potential μ in untwisted WSe₂/CrI₃ heterostructure, when $\theta_E = \pi/4$. It is found that the in-plane components of the intra-band spin polarization, S_x^{oc} and S_y^{oc} , are even with respect to the magnetization direction θ_m , whereas the out of plane component S_z^{oc} is odd function of θ_m and one order of magnitude larger than those of the in-plane components [see inset of Fig. 2(a)]. The spin polarization components exhibit strongly asymmetric behavior with respect to the chemical potential, without any change of sign.

As depicted in Fig. 2(c), the applied current-generated non-equilibrium spin polarization exerts an in-plane spin-orbit torque $\tau^{oc} = 2J\hbar^{-1}m_c(-S_y^{oc}, S_x^{oc}, 0)$, with respect to the WSe₂/CrI₃ bilayer, on the magnetization of the FM layer with

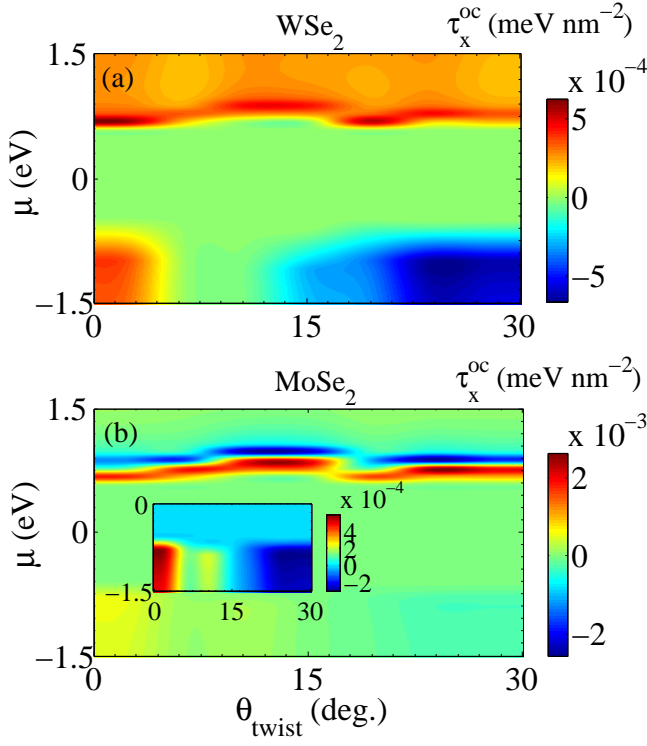


FIG. 3. (Color online) The colormap of the strength of the spin-orbit torque τ_x^{oc} as a function of the twist angle and the chemical potential for (a) $\text{WSe}_2/\text{CrI}_3$ and (b) $\text{MoSe}_2/\text{CrI}_3$ bilayers, when $\theta_m = 0$ and $\theta_E = \pi/4$. Inset of (b) shows the zoomed view of τ_x^{oc} in the case of p-doped MoSe_2 -based bilayer. The plots are interpolated from the data obtained in Ref. 40.

$\theta_m = 0$. Therefore, the even function of $S_{x(y)}^{oc}$ upon magnetization reversal makes the generated spin-orbit torque to act like a field-like torque (odd function with respect to θ_m). The x -component of the spin-orbit torque τ_x^{oc} (which is equal to τ_y^{oc} in the case of the applied current direction $\theta_E = \pi/4$) presents an asymmetric dependence on the chemical potential without any sign changes. Importantly, twisting the WSe_2 layer with respect to the ferromagnetic CrI_3 layer with the twist angle $\theta_{twist} = 30^\circ$ results in an amplification of the SOT as well as a sign change in p-doped WSe_2 -based bilayer. Comparing the results with that of the MoSe_2 -based bilayer demonstrate strong amplification of the magnitude of the SOT as well as its sign change in n-doped MoSe_2 -based structure in the absence or presence of twisting. We should note that the twist-angle induced sign change of the SOT in the case of p-type doping is also present in MoSe_2 -based bilayer. Most importantly, we show that the enhancement of the Rashba SOC not only leads to the strong amplification of the SOT in WSe_2 - and p-doped MoSe_2 -based structures, but also makes the SOT to decrease and change its sign in the case of n-doped $\text{MoSe}_2/\text{CrI}_3$ bilayer [see Fig. 2(d)]. Besides, we have found (not shown) that decreasing the temperature below the room temperature does not make any qualitative changes in chemical potential dependence of the current-induced spin polarization and generated

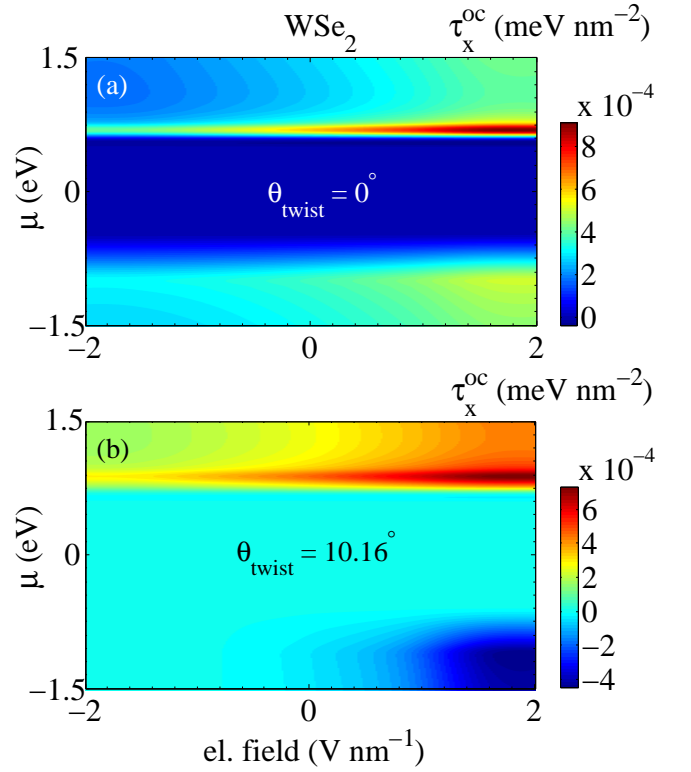


FIG. 4. (Color online) Dependence of the strength of the spin-orbit torque τ_x^{oc} on the gate electric field and the chemical potential for $\text{WSe}_2/\text{CrI}_3$ bilayer in the (a) absence and (b) presence of twisting (with $\theta_{twist} = 10.16^\circ$), when $\theta_m = 0$ and $\theta_E = \pi/4$. The plots are interpolated from the data obtained in Ref. 40.

spin-orbit torque components and leads to reduction of their magnitudes.

Most recently, the detailed study of the effect of twisting on the proximity exchange parameters done for intermediate twist angles shows that, depending on the relative twist angle, the band edge splittings can be markedly different and even the spin ordering can be reversed⁴⁰. In particular, when twisting from 0° to 30° , the TMDC conduction-band edge splitting remains nearly unchanged at around -3 meV. In contrast, there is a smooth transition of the TMDC valence-band edge spin-splitting in an almost linear fashion upon twisting (about -2 to 2 meV), and the twist angle at which the transition (the spin ordering changes) happens is identified about 8° (16°) for WSe_2 (MoSe_2). Furthermore, a giant tunability of the proximity-induced exchange coupling is provided by a transverse electric field of a few V/nm across the twisted TMDC/ CrI_3 bilayers. Motivated by this, we highlight the extraordinary tunability of the SOT by the effects of the twist-angle and gate electric-field in the following figures. We use the parameters obtained in Ref. 40 for 7 different twist angles between 0° and 30° , and interpolate the resulting plots using "bicubic" interpolation method.

To achieve qualitative understanding of how the SOT is influenced by twisting in a wide range of the twist angle, we

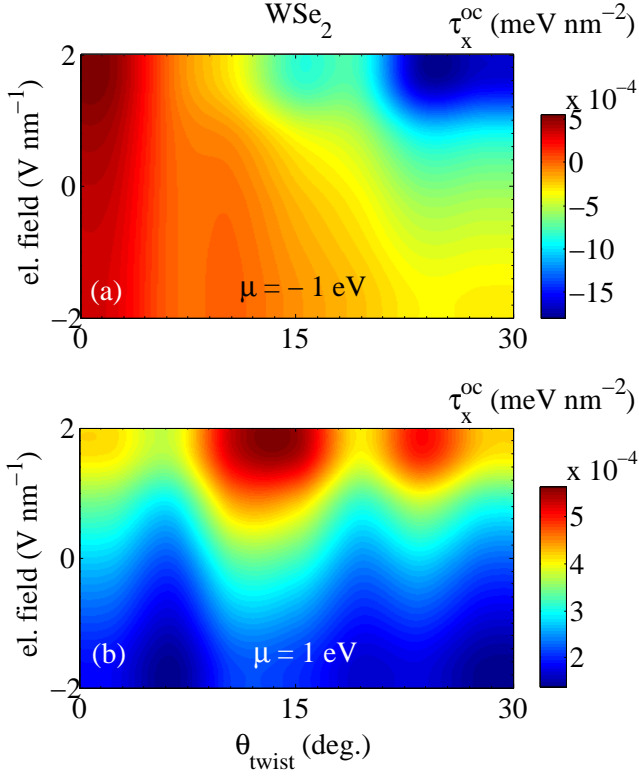


FIG. 5. (Color online) The colormap of the strength of the spin-orbit torque τ_x^{oc} as a function of the twist angle and the gate electric field for two values of the chemical potential (a) $\mu = -1$ eV and (b) $\mu = 1$ eV in $\text{WSe}_2/\text{CrI}_3$ bilayer, when $\theta_m = 0$ and $\theta_E = \pi/4$. The plots are interpolated from the data obtained in Ref. 40.

present the colormap of the strength of the x -component of the SOT as a function of the twist angle θ_{twist} and the chemical potential μ in Fig. 3 for WSe_2 - and MoSe_2 -based bilayers, when θ_m is set to zero, and $\theta_E = \pi/4$. A large discrepancy between the n-type and p-type doping can be apparently seen for both TMDC/ CrI_3 bilayers. Tuning the twist angle between 0° and 30° not only leads to significant changes in the magnitude of the SOT as well as a sign change in p-doped WSe_2 and MoSe_2 -based structures, but also can cause two sign changes in n-doped $\text{MoSe}_2/\text{CrI}_3$ bilayer. Most importantly, it is clear that the strength of the SOT in MoSe_2 -based bilayer is one order of magnitude larger than that of the WSe_2 -based bilayer. The large spin-splitting of the conduction and valence bands due to the intrinsic SOC, λ_c and λ_v , in comparison with those of proximity induced exchange coupling, B_c and B_v , are responsible for the large difference between the behavior of the SOT in two TMDCs, which have the same sign in WSe_2 - and different sign in $\text{MoSe}_2/\text{CrI}_3$ bilayers.

We further present the variation of τ_x^{oc} as a function of the gate electric field and the chemical potential for WSe_2 -based bilayer in the absence and presence of twisting (with $\theta_{twist} = 10.16^\circ$) in Fig. 4. Importantly, tuning the applied gate electric field from -2 V/nm to 2 V/nm not only enhances the strength of the SOT, but also leads to its sign change at the twist angle

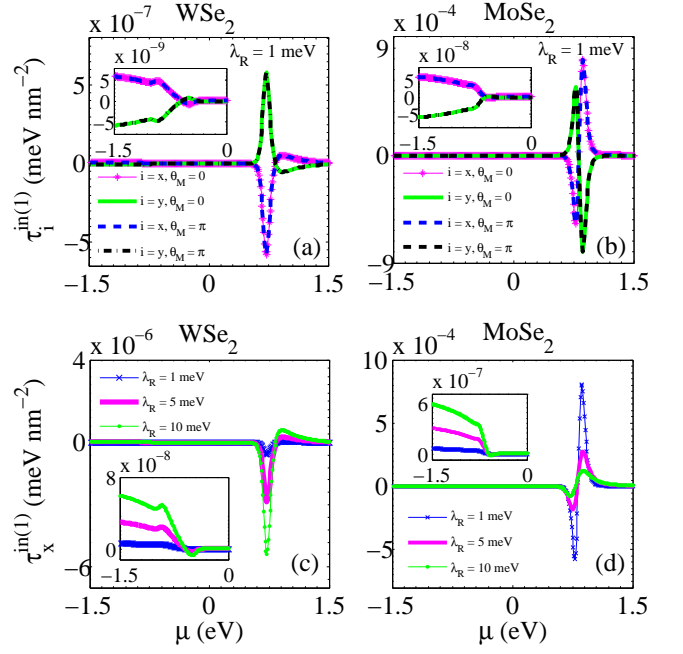


FIG. 6. (Color online) Chemical potential dependence of the intrinsic spin-orbit torque τ_x^{in} components in (a) $\text{WSe}_2/\text{CrI}_3$ and (b) $\text{MoSe}_2/\text{CrI}_3$ bilayers for two magnetization directions $\theta_m = 0$ and π , when $\lambda_R = 1$ meV, $\theta_{twist} = 0^\circ$ and $\theta_E = \pi/4$. The x -component of the intrinsic spin-orbit torque τ^{in} in terms of the chemical potential μ for three values of λ_R in (c) WSe_2 - and (d) MoSe_2 - based bilayers for $\theta_m = 0$, $\theta_{twist} = 0^\circ$ and $\theta_E = \pi/4$. Notice that we have $\tau_y^{oc} = \tau_x^{oc}$ in the case of $\theta_E = \pi/4$. The insets show the p-doped case.

$\theta_{twist} = 10.16^\circ$. This is due to the sign change of B_v occurring only in the case of $\theta_{twist} = 10.16^\circ$. Meanwhile, tuning the gate electric field at other twist angles leads to the amplification of the strength of the exchange coupling in the conduction and valence bands.

Moreover, the striking tunability of the SOT by the effects of the twist angle and gate electric field is depicted in Fig. 5 for WSe_2 -based bilayer with n- or p-type doping. Remarkably, the sign change of the SOT as well as a significant amplification of its strength can be achieved for a wide window of the twist angle and the gate electric field in p-doped bilayer and the strength of the SOT is in the same order as n-type doping.

B. Spin-orbit torque from inter-band transitions

As is evident from Figs. 6 (a) and (b), the intrinsic in-plane SOT is even with respect to the magnetization direction θ_m (intrinsic spin polarization is odd) as expected from a damping-like term. We can see that similar to the field-like term, the intrinsic SOT is much smaller in the p-doped case with respect to that of the n-doped in both systems. On the other hand, the magnitude of the intrinsic SOT in the case of using MoSe_2 is larger than WSe_2 and it is approximately at the same

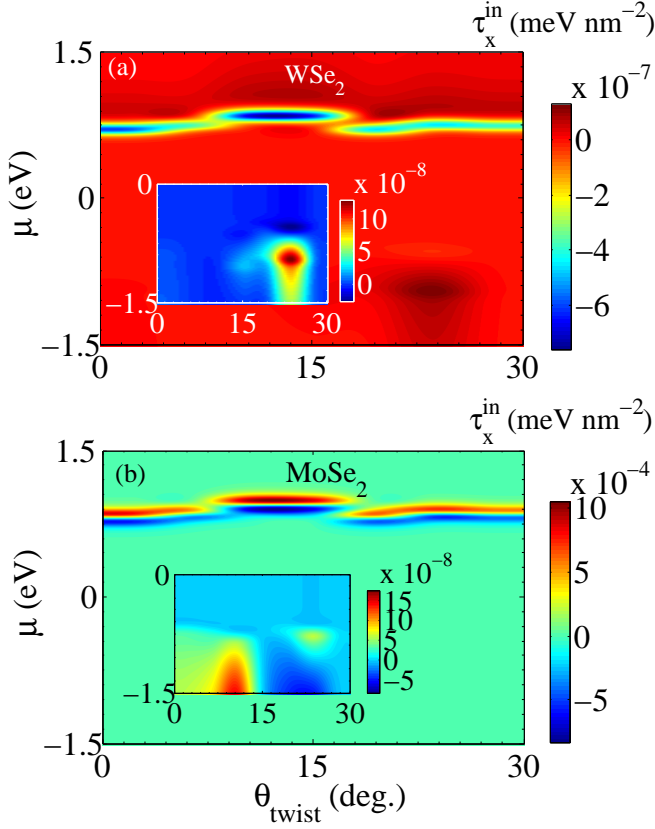


FIG. 7. (Color online) The colormap of the strength of the intrinsic spin-orbit torque τ_x^{in} as a function of the twist angle and the chemical potential for (a) $\text{WSe}_2/\text{CrI}_3$ and (b) $\text{MoSe}_2/\text{CrI}_3$ bilayers, when $\theta_m = 0$ and $\theta_E = \pi/4$. The insets show the p-doped case. The plots are interpolated from the data obtained in Ref. 40.

order of the field-like term. Changing the chemical potential of the system, a sign change in the intrinsic SOT is seen which is more pronounced for the n-doped cases.

We have also compared the intrinsic SOT for both n- and p-doped cases in both systems for different values of Rashba spin-orbit coupling, λ_R in Figs. 6 (c) and (d). The interesting point here is that for larger values of λ_R , the intrinsic SOT increases considerably in all cases except the n-doped MoSe_2 for which the larger torque belongs to the smaller λ_R . This can be attributed to the negative value of spin-orbit coupling, λ_c in the conduction band of MoSe_2 such that the conduction band of MoSe_2 with spin up is lower in energy than the one with spin down.

The intrinsic SOT is also strongly affected by twisting of the ferromagnetic layer. As seen in Fig. 7, the magnitude of the torque can be abruptly altered under twisting such that for some energies and for certain twist angles (depending on the material and n- or p-doping), the change is larger than one order of magnitude. More importantly, here also twisting can lead to a sign change in the intrinsic SOT for both MoSe_2 and WSe_2 in n- and p-doped cases.

There is also a possibility for tuning the magnitude and the

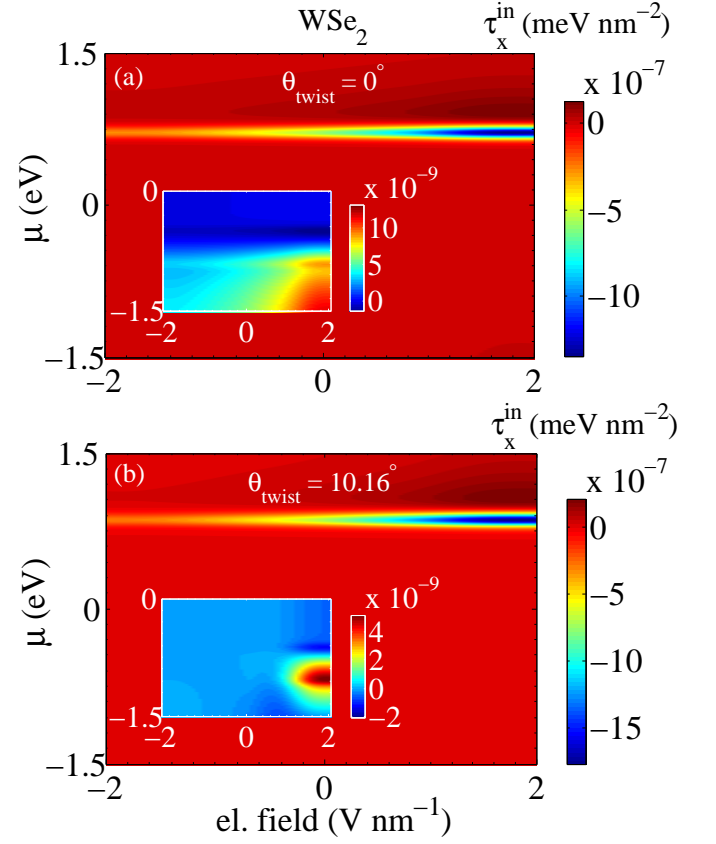


FIG. 8. (Color online) The colormap of the strength of the intrinsic spin-orbit torque τ_x^{in} as a function of the gate electric field and the chemical potential for $\text{WSe}_2/\text{CrI}_3$ bilayer in the (a) absence and (b) presence of twisting (with $\theta_{\text{twist}} = 10.16^\circ$), when $\theta_m = 0$ and $\theta_E = \pi/4$. The insets show the p-doped case. The plots are interpolated from the data obtained in Ref. 40.

sign of the intrinsic SOT applying a gate voltage in the system. In Fig. 8, we have shown the results of our calculation for five distinct values of the electric field and for two cases: with no twist and a 10.16° twist. The electric field directly affects the proximity exchange parameters B_c and B_v . While for all twists a gate scan from -2 V/nm to 2 V/nm only increases the absolute value of the exchange parameters, there is a sign change in B_v for the special case of $\theta_{\text{twist}} = 10.16^\circ$. The intrinsic SOT also follows the changes in proximity parameters such that a gate scan from -2 V/nm to 2 V/nm increases the magnitude of the torque in n-doped systems for both 0° and 10.16° twist and also in p-doped case for 0° twist. In the case of p-doped system with 10.16° twist, we find that gating can change the sign of the torque as well. In Fig. 9, we can see the tunability of the intrinsic SOT as a function of the electric field and the twist angle for $\mu = -1.5 \text{ eV}$ in p-doped and $\mu = 0.9 \text{ eV}$ in n-doped case. We should note that since the intrinsic SOT is much smaller than its counterpart arising from the intra-band transitions, the second-order response is negligible in this case and can therefore be safely ignored⁵⁸.

We also evaluate the results in the absence of Rashba SOC

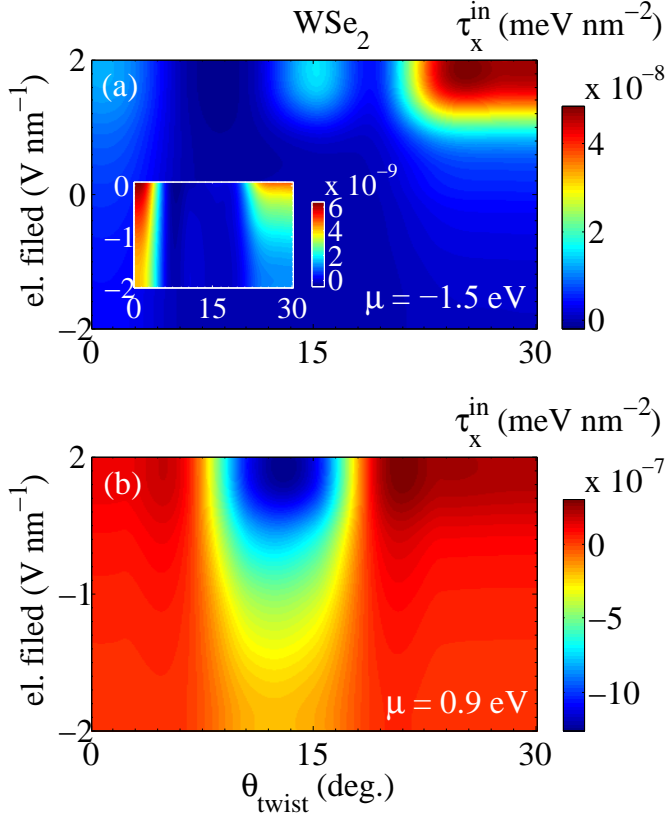


FIG. 9. (Color online) The colormap of the strength of the intrinsic spin-orbit torque τ_x^{in} as a function of the twist angle and the gate electric field for two values of the chemical potential (a) $\mu = -1.5$ eV and (b) $\mu = 0.9$ eV in $\text{WSe}_2/\text{CrI}_3$ bilayer, when $\theta_m = 0$ and $\theta_E = \pi/4$. Inset of (a) shows the negative gate electric field case. The plots are interpolated from the data obtained in Ref. 40.

parameter. Importantly, we find that the contribution of the intrinsic inter-band and intra-band transitions is zero in linear response regime, and the non-linear spin polarization associated with intra-band transitions generates a strong in-plane field-like spin-orbit torque $\tau^{\text{oc}} = 2J\hbar^{-1}(m_z S_x^{\text{oc}} - m_x S_z^{\text{oc}}) \hat{y}$, on the ferromagnetic CrI_3 layer. Remarkably, the non-linear field-like torque is one order of magnitude larger than that of the linear SOT in the presence of Rashba SOC. As depicted in Fig. 10, SOT has asymmetric dependence on the chemical potential with larger value in the case of n-type doping and changes sign for MoSe_2 - and p-type doped WSe_2 -based bilayers, in contrast to the case with finite Rashba SOC. Twisting the TMDC layer with respect to the ferromagnetic CrI_3 layer results in an amplification or attenuation of the strength of the SOT depending on the chemical potential as well as a sign change in n-type doped WSe_2 -based bilayer. Moreover, the strength of the spin-orbit torque in MoSe_2 -based bilayer with n-type doping is found to be one order of magnitude larger than that of the $\text{WSe}_2/\text{CrI}_3$ bilayer. We additionally find that the SOT is insensitive to the direction of the applied in-plane electric field, in contrast to the case with finite Rashba.

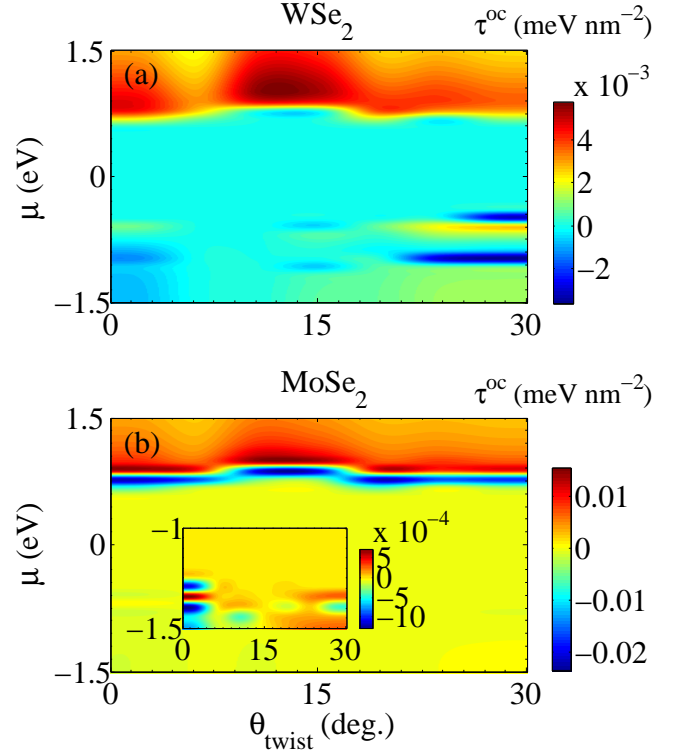


FIG. 10. (Color online) The colormap of the strength of the spin-orbit torque τ^{oc} as a function of the twist angle and the chemical potential for (a) $\text{WSe}_2/\text{CrI}_3$ and (b) $\text{MoSe}_2/\text{CrI}_3$ bilayers, when $\lambda_R = 0$, $\theta_m = \pi/4$ and $\theta_E = \pi/4$. Inset of (b) shows the zoomed in view of τ_x^{oc} in the case of p-doped MoSe_2 -based bilayer. The plots are interpolated from the data obtained in Ref. 40.

IV. CONCLUSION

In summary, we have studied the current-induced spin polarization and the resulting spin-orbit torque (SOT) in a transition metal dichalcogenide (TMDC) and chromium iodide (CrI_3) bilayer, with WSe_2 or MoSe_2 as TMDC, beyond the linear response theory. Employing the single-band steady state Boltzmann equation, we have found that the spin-polarization originating from the electron occupation changes within intra-band is odd upon magnetization reversal and generates a strong field-like SOT, τ^{oc} , on the magnetization of the ferromagnetic CrI_3 layer, while that of the intrinsic inter-band transitions contribute to a weak damping-like torque, τ^{in} , in TMDC/ CrI_3 bilayers. Both the field-like and damping-like terms exhibit strongly asymmetric behavior with respect to the chemical potential with higher strength in the case of n-type doping and sign changes for n-doped $\text{MoSe}_2/\text{CrI}_3$ bilayers.

We have evaluated the effects of the type of the TMDC, twisting the TMDC layer with respect to the CrI_3 , and the gate electric field on the generated SOT. Interestingly, the strength of the damping-like (field-like) SOT in MoSe_2 -based bilayer can be three orders (one order) of magnitude larger than that of the WSe_2 -based bilayer, leading to an approximately the

same order as the field-like torque. Moreover, the field-like and damping-like SOTs are enhanced for larger Rashba spin-orbit couplings in WSe₂- and p-type doped MoSe₂-based bilayers, whereas their strengths are reduced in n-doped MoSe₂ and the sign change of the field-like torque is disappeared.

Twisting the TMDC layer with respect to the ferromagnetic CrI₃ layer, which is accompanied by reversal of the spin ordering, leads to significant changes in applied current-induced SOTs. Importantly, a large discrepancy between the n-type and p-type doping can be apparently seen in WSe₂ and MoSe₂-based bilayers. Not only do the magnitudes of the SOTs can change significantly, but also the sign of the damping-like SOT as well as the field-like SOT (except that of the n-doped WSe₂) can be reversed by tuning the twist angle between 0° and 30° in both TMDCs.

Furthermore, tuning the applied gate electric field from -2 V/nm to 2 V/nm can lead to the sign change of the SOTs in addition to the amplification of their strengths. Most importantly, we have depicted the striking tunability of the strength of the generated SOTs as well as their sign change in a wide window of the twist angle and the applied gate electric field which opens a new path for externally controllable spintronic devices.

Since several works in the field of SOTs using TMDC-based devices are available, a proper comparison with those results seems to be in order. Experimental studies show that various factors- including the source of TMDCs (e.g., mechanical exfoliation or chemical vapor deposition), the choice of ferromagnetic materials (FM), deposition techniques (such as sputtering or electron-beam evaporation), and measurement techniques like second-harmonic Hall (SHH)⁵⁹⁻⁶² or spin-torque ferromagnetic resonance (ST-FMR)⁶³⁻⁶⁵ affect the measured SOTs.

Shao *et al.* reported an absence of in-plane damping-like torque and a temperature-independent out of plane field-like torque $\tau_{FL} \sim 10^{-7}$ (10^{-8}) meV/nm² in monolayer WSe₂ (MoS₂) coupled with CoFeB, quantified using non-resonant SHH measurements²⁸. Interestingly, in a concurrent study, Zhang *et al.* obtained different results using a high-frequency technique, ST-FMR, on monolayer

MoS₂/Permalloy (Ni₈₀Fe₂₀-Py)²⁷ and detected both in-plane damping-like and out-of-plane field-like torques, with a torque ratio of $\tau_{FL}/\tau_{DL} = 0.19 \pm 0.01$, indicating that the damping-like torque dominates over the field-like torque. Crucially, this result repeated using different deposition techniques of the FM layer deposition methods, indicating that the observed torque is not affected by the Py deposition technique. While different measurement techniques might explain the discrepancy in the observed torques, it has been demonstrated that SOT values quantified by ST-FMR and SHH techniques are typically in good agreement within experimental accuracy across several systems^{22,25,66}. The conflicting findings in MoS₂/FM bilayers highlight that not only the spin-orbit material but also the type of ferromagnetic layer plays a significant role in the resulting torque characteristics. This is theoretically supported by recent calculations on heterostructures such as MoSe₂/Co, WSe₂/Co, and TaSe₂/Co³³. Moreover, Lv *et al.* observed both damping-like and field-like torques in ST-FMR measurements on monolayer WS₂/Py heterostructures³⁶, using CVD-grown WS₂ and electron-beam evaporated Py, attributed to the interfacial Rashba-Edelstein effect. Notably, they observed a gate-dependent SOT ratio ranging from $\tau_{FL}/\tau_{DL} = 0.05$ to 0.22 within a range of -60 V to +60 V, an effect absent in their Pt/Py reference samples.

To the best of our knowledge, this is the first report to explore SOT in TMDCs interfaced with two-dimensional (2D) FM CrI₃, revealing both field-like and damping-like torque components. Remarkably, the strength of both field-like and damping-like torques are at least three orders of magnitudes larger than previously reported results. The obtained spin torques ratio τ_{FL}/τ_{DL} , reaching approximately 10^3 for WSe₂ and 10 for MoSe₂, exceed prior studies by two to four orders of magnitude. It is worth noting that the predicted magnitudes of the spin torques and the resulting τ_{FL}/τ_{DL} ratio in MoSe₂/CrI₃ bilayer are comparable to those obtained in TI/2D FM bilayer with a value of approximately $\tau_{FL}/\tau_{DL} \sim 10^{-3}/10^{-4} = 10$ ⁶⁷, whereas the corresponding ratio in WSe₂-based bilayer is significantly higher than the value reported in TI/2D FM system. These findings highlight CrI₃ as a highly promising 2D FM for externally controllable spintronic devices.

* Leyla.Majidi@gmail.com; l.majidi@scu.ac.ir

¹ J. C. Slonczewski, J. Magn. Magn. Mater **159**, L1 (1996).

² L. Berger, Phys. Rev. B **54**, 9353 (1996).

³ E. Myers, D. Ralph, J. Katine, R. Louie, and R. Buhrman, Science **285**, 867 (1999).

⁴ J. Katine, F. Albert, R. Buhrman, E. Myers, and D. Ralph, Phys. Rev. Lett. **84**, 3149 (2000).

⁵ M. Zare, L. Majidi, and R. Asgari, Phys. Rev. B **95**, 115426 (2017).

⁶ L. Majidi, M. Zare, and R. Asgari, Physica C **549**, 77 (2018).

⁷ V. P. Amin, J. Zemen, and M. D. Stiles, Phys. Rev. Lett. **121**, 136805 (2018).

⁸ P. Gambardella and I. M. Miron, Philos. Trans. R. Soc. A Math. Phys. Eng. Sci. **369**, 3175 (2011).

⁹ A. Manchon, J. Železný, I. M. Miron, T. Jungwirth, J. Sinova, A. Thiaville, K. Garello, and P. Gambardella, Rev. Mod. Phys. **91**, 035004 (2019).

¹⁰ L. Liu, C.-F. Pai, Y. Li, H. Tseng, D. Ralph, and R. Buhrman, Science **336**, 555 (2012).

¹¹ L. Liu, O. Lee, T. Gudmundsen, D. Ralph, and R. Buhrman, Phys. Rev. Lett. **109**, 096602 (2012).

¹² C.-F. Pai, M.-H. Nguyen, C. Belvin, L. H. Vilela-Leão, D. Ralph, and R. Buhrman, Appl. Phys. Lett. **104**, 082407 (2014).

¹³ T. D. Skinner, K. Olejník, L. Cunningham, H. Kurebayashi, R. Campion, B. Gallagher, T. Jungwirth, and A. J. Ferguson, Nat. Commun. **6**, 6730 (2015).

¹⁴ Y. Fan, P. Upadhyaya, X. Kou, M. Lang, S. Takei, Z. Wang, J. Tang, L. He, L.-T. Chang, M. Montazeri, *et al.*, Nat. Mater. **13**,

- 699 (2014).
- ¹⁵ Y. Wang, P. Deorani, K. Banerjee, N. Koirala, M. Brahlek, S. Oh, and H. Yang, *Phys. Rev. Lett.* **114**, 257202 (2015).
 - ¹⁶ K. Kondou, R. Yoshimi, A. Tsukazaki, Y. Fukuma, J. Matsuno, K. Takahashi, M. Kawasaki, Y. Tokura, and Y. Otani, *Nat. Phys.* **12**, 1027 (2016).
 - ¹⁷ J. Han, A. Richardella, S. A. Siddiqui, J. Finley, N. Samarth, and L. Liu, *Phys. Rev. Lett.* **119**, 077702 (2017).
 - ¹⁸ Y. Liu and Q. Shao, *ACS Nano* **14**, 9389 (2020).
 - ¹⁹ J. Hidding and M. H. Guimarães, *Front. Mater.* **7**, 594771 (2020).
 - ²⁰ W. Tang, H. Liu, Z. Li, A. Pan, and Y.-J. Zeng, *Adv. Sci.* **8**, 2100847 (2021).
 - ²¹ R. Galceran, B. Tian, J. Li, F. Bonell, M. Jamet, C. Vergnaud, A. Marty, J. H. García, J. F. Sierra, M. V. Costache, *et al.*, *APL Mater* **9**, 100901 (2021).
 - ²² D. MacNeill, G. Stiehl, M. Guimaraes, R. Buhrman, J. Park, and D. Ralph, *Nat. Phys.* **13**, 300 (2017).
 - ²³ P. Li, W. Wu, Y. Wen, C. Zhang, J. Zhang, S. Zhang, Z. Yu, S. A. Yang, A. Manchon, and X.-x. Zhang, *Nat. Commun.* **9**, 3990 (2018).
 - ²⁴ B. Zhao, D. Khokhriakov, Y. Zhang, H. Fu, B. Karpiak, A. M. Hoque, X. Xu, Y. Jiang, B. Yan, and S. P. Dash, *Phys. Rev. Res.* **2**, 013286 (2020).
 - ²⁵ G. M. Stiehl, D. MacNeill, N. Sivadas, I. El Baggari, M. H. Guimaraes, N. D. Reynolds, L. F. Kourkoutis, C. J. Fennie, R. A. Buhrman, and D. C. Ralph, *ACS Nano* **13**, 2599 (2019).
 - ²⁶ A. M. Hoque, D. Khokhriakov, B. Karpiak, and S. P. Dash, *Phys. Rev. Res.* **2**, 033204 (2020).
 - ²⁷ W. Zhang, J. Sklenar, B. Hsu, W. Jiang, M. B. Jungfleisch, J. Xiao, F. Y. Fradin, Y. Liu, J. E. Pearson, J. B. Ketterson, *et al.*, *APL Mater* **4**, 032302 (2016).
 - ²⁸ Q. Shao, G. Yu, Y.-W. Lan, Y. Shi, M.-Y. Li, C. Zheng, X. Zhu, L.-J. Li, P. K. Amiri, and K. L. Wang, *Nano Lett.* **16**, 7514 (2016).
 - ²⁹ S. Novakov, B. Jariwala, N. M. Vu, A. Kozhakhmetov, J. A. Robinson, and J. T. Heron, *ACS Appl. Mater. Interfaces* **13**, 13744 (2021).
 - ³⁰ J. Hidding, S. H. Tirion, J. Momand, A. Kaverzin, M. Mostovoy, B. J. Van Wees, B. J. Kooi, and M. H. Guimarães, *J. Phys. Mater.* **4**, 04LT01 (2021).
 - ³¹ M. H. Guimaraes, G. M. Stiehl, D. MacNeill, N. D. Reynolds, and D. C. Ralph, *Nano Lett.* **18**, 1311 (2018).
 - ³² S. Husain, X. Chen, R. Gupta, N. Behera, P. Kumar, T. Edvinsson, F. Garcia-Sanchez, R. Brucas, S. Chaudhary, B. Sanyal, *et al.*, *Nano Lett.* **20**, 6372 (2020).
 - ³³ K. Dolui and B. K. Nikolić, *Phys. Rev. Mater.* **4**, 104007 (2020).
 - ³⁴ A. Manchon and S. Zhang, *Phys. Rev. B* **79**, 094422 (2009).
 - ³⁵ R. Mishra, F. Mahfouzi, D. Kumar, K. Cai, M. Chen, X. Qiu, N. Kioussis, and H. Yang, *Nat. Commun.* **10**, 248 (2019).
 - ³⁶ W. Lv, Z. Jia, B. Wang, Y. Lu, X. Luo, B. Zhang, Z. Zeng, and Z. Liu, *ACS Appl. Mater. Interfaces* **10**, 2843 (2018).
 - ³⁷ X. Lin and L. Zhu, *Mater. Today Electron.* **4**, 100037 (2023).
 - ³⁸ K. Zollner, P. E. Faria Junior, and J. Fabian, *Phys. Rev. B* **100**, 085128 (2019).
 - ³⁹ L. Majidi and R. Asgari, *Phys. Rev. B* **106**, 045406 (2022).
 - ⁴⁰ K. Zollner, P. E. Faria Junior, and J. Fabian, *Phys. Rev. B* **107**, 035112 (2023).
 - ⁴¹ S. Jiang, L. Li, Z. Wang, K. F. Mak, and J. Shan, *Nat. Nanotechnol.* **13**, 549 (2018).
 - ⁴² J. Kim, K.-W. Kim, B. Kim, C.-J. Kang, D. Shin, S.-H. Lee, B.-C. Min, and N. Park, *Nano Lett.* **20**, 929 (2019).
 - ⁴³ C. Lei, B. L. Chittari, K. Nomura, N. Banerjee, J. Jung, and A. H. MacDonald, *Nano Lett.* **21**, 1948 (2021).
 - ⁴⁴ P. Zhang, T.-F. Chung, Q. Li, S. Wang, Q. Wang, W. L. Huey, S. Yang, J. E. Goldberger, J. Yao, and X. Zhang, *Nat. Mater.* **21**, 1373 (2022).
 - ⁴⁵ D. Zhong, K. L. Seyler, X. Linpeng, R. Cheng, N. Sivadas, B. Huang, E. Schmidgall, T. Taniguchi, K. Watanabe, M. A. McGuire, *et al.*, *Sci. Adv.* **3**, e1603113 (2017).
 - ⁴⁶ K. L. Seyler, D. Zhong, B. Huang, X. Linpeng, N. P. Wilson, T. Taniguchi, K. Watanabe, W. Yao, D. Xiao, M. A. McGuire, *et al.*, *Nano Lett.* **18**, 3823 (2018).
 - ⁴⁷ T. Hu, G. Zhao, H. Gao, Y. Wu, J. Hong, A. Stroppa, and W. Ren, *Phys. Rev. B* **101**, 125401 (2020).
 - ⁴⁸ M. Ge, H. Wang, J. Wu, C. Si, J. Zhang, and S. Zhang, *npj Comput. Mater.* **8**, 32 (2022).
 - ⁴⁹ K. Dolui, M. D. Petrovic, K. Zollner, P. Plechac, J. Fabian, and B. K. Nikolić, *Nano Lett.* **20**, 2288 (2020).
 - ⁵⁰ M.-C. Heißenbuttel, T. Deilmann, P. Krüger, and M. Rohlfing, *Nano Lett.* **21**, 5173 (2021).
 - ⁵¹ M. Dabrowski, S. Guo, M. Strungaru, P. S. Keatley, F. Withers, E. J. Santos, and R. J. Hicken, *Nat. Commun.* **13**, 5976 (2022).
 - ⁵² H. Kurebayashi, J. Sinova, D. Fang, A. C. Irvine, T. D. Skinner, J. Wunderlich, V. Novk, V. Campion, B. L. Gallagher, E. K. Vehstedt, L. P. Zørbo, K. Vbörn, A. J. Ferguson, and T. Jungwirth, *Nature Nanotechnology* **9**, 211217 (2014).
 - ⁵³ C. Xiao and Q. Niu, *Phys. Rev. B* **96**, 045428 (2017).
 - ⁵⁴ I. Garate and A. H. MacDonald, *Phys. Rev. B* **80**, 134403 (2009).
 - ⁵⁵ B. Radisavljevic, A. Radenovic, J. Brivio, V. Giacometti, and A. Kis, *Nat. Nanotechnol.* **6**, 147150 (2011).
 - ⁵⁶ M. Fontana, T. Deppe, A. K. Boyd, M. Rinzan, A. Y. Liu, M. Paranjape, and P. Barbara, *Scientific Reports* **3**, 1634 (2013).
 - ⁵⁷ M. R. Laskar, D. N. Nath, L. Ma, E. W. Lee II, C. H. Lee, T. Kent, Z. Yang, R. Mishra, M. Roldan, A. J.-C. Idrobo, S. T. Pantelides, S. J. Pennycook, R. C. Myers, Y. Wu, and S. Rajan, *Appl. Phys. Lett.* **104**, 092104 (2014).
 - ⁵⁸ Y.-L. Zhou, H.-J. Duan, Y.-j. Wu, M.-X. Deng, L. Wang, D. Culcer, and R.-Q. Wang, *Phys. Rev. B* **105**, 075415 (2022).
 - ⁵⁹ K. Garello, I. M. Miron, C. O. Avci, F. Freimuth, Y. Mokrousov, S. Blügel, S. Auffret, O. Boulle, G. Gaudin, and P. Gambardella, *Nat. Nanotechnol.* **8**, 587 (2013).
 - ⁶⁰ M. Hayashi, J. Kim, M. Yamanouchi, and H. Ohno, *Phys. Rev. B* **89**, 144425 (2014).
 - ⁶¹ C. O. Avci, K. Garello, M. Gabureac, A. Ghosh, A. Fuhrer, S. F. Alvarado, and P. Gambardella, *Phys. Rev. B* **90**, 224427 (2014).
 - ⁶² A. Ghosh, K. Garello, C. O. Avci, M. Gabureac, and P. Gambardella, *Phys. Rev. Appl.* **7**, 014004 (2017).
 - ⁶³ L. Liu, T. Moriyama, D. C. Ralph, and R. A. Buhrman, *Phys. Rev. Lett.* **106**, 036601 (2011).
 - ⁶⁴ D. Fang, H. Kurebayashi, J. Wunderlich, K. Vbörn, L. P. Zørbo, R. P. Campion, A. Casiraghi, B. L. Gallagher, T. Jungwirth, and A. J. Ferguson, *Nat. Nanotechnol.* **6**, 413 (2011).
 - ⁶⁵ A. J. Berger, E. R. J. Edwards, H. T. Nembach, A. D. Karenowska, M. Weiler, and T. J. Silva, *Phys. Rev. B* **97**, 094407 (2018).
 - ⁶⁶ S. Shi, S. Liang, Z. Zhu, K. Cai, S. D. Pollard, Y. Wang, J. Wang, Q. Wang, P. He, J. Yu, G. Eda, G. Liang, and H. Yang, *Nat. Nanotechnol.* **14**, 945 (2019).
 - ⁶⁷ S. Ghosh and A. Manchon, *Phys. Rev. B* **95**, 035422 (2017).